molecules

MDPI

Article

Single-Layer $GaInSe_3$: Promising Water-Splitting Photocatalyst with Solar Conversion Efficiency over 30% from Theoretical Calculations

Li-Li Liu [1,2,*], Ru-Fei Tang [1], De-Fen Li [1], Ming-Xia Tang [1], Bing-Zhong Mu [1], Zheng-Quan Hu [3], Shi-Fa Wang [3], Yu-Feng Wen [4,*] and Xiao-Zhi Wu [2]

[1] College of Teacher Education, Chongqing Three Gorges University, Chongqing 404100, China; TangRFsanxu@163.com (R.-F.T.); LiDFsanxu@163.com (D.-F.L.); tangmxsanxu@163.com (M.-X.T.); m15213132982@163.com (B.-Z.M.)
[2] Institute for Structure and Function, Chongqing University, Chongqing 401331, China; xiaozhiwu@cqu.edu.cn
[3] College of Electronic and Information Engineering, Chongqing Three Gorges University, Chongqing 404100, China; hzq250314@163.com (Z.-Q.H.); wangshifa2006@yeah.net (S.-F.W.)
[4] School of Mathematical Sciences and Physics, Jinggangshan University, Ji'an 343009, China
* Correspondence: liulili0612@163.com (L.-L.L.); wenyufeng@jgsu.edu.cn (Y.-F.W.)

Abstract: Hydrogen energy from solar water-splitting is known as an ideal method with which to address the energy crisis and global environmental pollution. Herein, the first-principles calculations are carried out to study the photocatalytic water-splitting performance of single-layer $GaInSe_3$ under biaxial strains from −2% to +2%. Calculations reveal that single-layer $GaInSe_3$ under various biaxial strains has electronic bandgaps ranging from 1.11 to 1.28 eV under biaxial strain from −2% to +2%, as well as a completely separated valence band maximum and conduction band minimum. Meanwhile, the appropriate band edges for water-splitting and visible optical absorption up to ~3×10^5 cm^{-1} are obtained under biaxial strains from −2% to 0%. More impressively, the solar conversion efficiency of single-layer $GaInSe_3$ under biaxial strains from −2% to 0% reaches over 30%. The OER of unstrained single-layer $GaInSe_3$ can proceed without co-catalysts. These demonstrate that single-layer $GaInSe_3$ is a viable material for solar water-splitting.

Keywords: 2D material; single-layer $GaInSe_3$; water-splitting; strain engineering; solar energy

Citation: Liu, L.-L.; Tang, R.-F.; Li, D.-F.; Tang, M.-X.; Mu, B.-Z.; Hu, Z.-Q.; Wang, S.-F.; Wen, Y.-F.; Wu, X.-Z. Single-Layer $GaInSe_3$: Promising Water-Splitting Photocatalyst with Solar Conversion Efficiency over 30% from Theoretical Calculations. *Molecules* **2023**, *28*, 6858. https://doi.org/10.3390/molecules28196858

Academic Editor: Bryan M. Wong

Received: 7 August 2023
Revised: 13 September 2023
Accepted: 25 September 2023
Published: 28 September 2023

1. Introduction

With the development of human society and economy, the demand and consumption of energy have become unprecedented, and the environmental problems caused by the exploitation and consumption of traditional energy are prominently increasing. Therefore, it is urgent to seek a new source of energy which does not produce pollution in the production and utilization processes. Hydrogen with high calorific value and pollution-free combustion has become the first choice for future energy. Hydrogen energy from efficient and environmentally friendly solar water-splitting has become an ideal method by which to solve our energy-related problems. During the early years of this research, semiconductor oxides such as TiO_2, ZnO, and SnO_2 were focused on [1–3]. However, the solar-to-hydrogen (STH) conversions of these semiconductor oxides are very limited due to the high recombination rates of charge carriers and low sunlight absorption [4,5]. Hence, reducing the recombination rates of carriers and enhancing solar absorption are two main approaches to improving STH conversions. As compared with traditional semiconductor oxides, two-dimensional (2D) materials possess low carrier recombination rates due to shorter carrier migration distances [6–8]. Meanwhile, for 2D materials, since the active potential is rich, the performance of sunlight absorption is strong, and the structural characteristics (such as planar, curved, vertically symmetric, or asymmetrical structures) are diverse, two-dimensional layered materials have been rapidly developed in photocatalytic water-splitting for hydrogen production [6–8]. Since solar absorption is directly

related to the bandgap, reducing the bandgap is an effective approach to enhancing optical absorption. After the inclusion of electric dipoles (fields), the bandgaps of 2D photocatalysts may decrease to ~0.5 eV [9]. Hence, the inside electric field not only enhances the optical absorption but also effectively reduces the recombination of carriers [10,11].

Single-layer M_2X_3 (M = Ga, In; X = S, Se, Te) are a typical group of 2D semiconductors with inside electric fields [12,13]. In_2X_3 (X = S, Se, Te) is an indirect bandgap semiconductor with good performance in photocatalytic water-splitting. Single-layer Ga_2X_3 (X = S, Se, Te) has better performance of in water-splitting and higher hydrogen production. It has been found that single-layer M_2X_3 (M = Ga, In; X = S, Se, Te) has excellent solar water-splitting performance owing to separated charge carriers [10,11]. After the anions in single-layer M_2X_3 are replaced, the STH conversion is enhanced [9]. Moreover, the bandgap, band edge position, and sunlight absorption of single-layer chalcogenide can be adjusted via biaxial strain, thereby improving the solar energy conversion efficiency [1–3]. In recent years, due to the successful synthesis of vertically asymmetric monolayers Janus MoSSe [14], Janus 2D materials have become a new research hotspot in the field of photocatalysis. The structural, electronic, and transport properties of single-layer $GaInX_3$ (X = S, Se, Te) were predicted via first-principles calculations [15]. Single-layer $GaInX_3$ were found to have structural stability, highly directional isotropic elasticity, a distinct vacuum level difference, and highly directional isotropic mobility; hence, they are candidates for applications in nanoelectronic devices [15]. In particular, we should note that a direct bandgap of 1.20 eV for single-layer $GaInSe_3$ indicates its visible and infrared light absorption [15]. Moreover, as a sulfur-free compound, single-layer $GaInSe_3$ is environmentally friendly. Consequently, it would be meaningful to investigate the solar water-splitting performance of single-layer $GaInSe_3$.

In this work, the solar water-splitting property of single-layer $GaInSe_3$ is calculated by the first-principles method. Since water-splitting can be effectively affected via biaxial strain [16,17], we also apply biaxial strains from −2% to 2% to tune the solar water-splitting property. Theoretical calculations suggest that under biaxial strains from −2% to 0%, single-layer $GaInSe_3$ has appropriate band edges for water-splitting and visible optical absorption up to ~3×10^5 cm^{-1}. Impressively, the STH efficiency of single-layer $GaInSe_3$ under biaxial strains from −2% to 0% surpasses 30%, demonstrating the potential applications of single-layer $GaInSe_3$ as a solar water-splitting material.

2. Computational Details

First-principles calculations are performed within the framework of the density functional theory (DFT) via the Vienna ab initio simulation package (VASP) [18–20]. The interaction between the core and valence electrons is treated via the projector-augmented wave (PAW) method [21,22], and the Perdew–Burke–Ernzerhof generalized gradient approximation (GGA-PBE) is used to describe the exchange and correlation potential [23]. The k-point mesh size with 11 × 11 × 1 and a cutoff energy of 500 eV are employed to optimize the structural parameter. The vacuum thickness of ~20 Å is added to avoid the interlayer reaction between repeated images, and the van der Waals (vdW) interlayer interaction is described using the semi-empirical DFT-D3 method [24]. The energy and force convergences are set as 10^{-7} eV and 0.01 eV/Å, respectively. Because the GGA-PBE usually underestimates the band gaps, the HSE06 method [25–27] and the G_0W_0 method [28] are both used to calculate band structures. Phonon dispersion curves are computed within a 4 × 4 × 1 supercell approach using the density functional perturbation theory [29] and extracted via the Phonopy code [30,31]. In ab initio molecular dynamics (AIMD) simulations, the initial configuration within the 3 × 3 × 1 supercell is annealed at 300 K in the NVT ensemble, and each AIMD simulation lasts for 8 ps, with a time step of 1 fs. The elastic constants are calculated using the finite different method [29].

To obtain the optical absorption, the 8 × 8 × 1 *k*-point grid is sampled in the G_0W_0 + BSE calculations [32–35]. (1) GGA-PBE calculations with an energy convergence criterion of 1×10^{-8} eV are performed; (2) GGA-PBE calculations are restarted to allow for full optical transitions, where ~200 empty bands are added; (3) G_0W_0 calculations are

carried out to obtain quasi-particle excitations, where an energy cutoff of 150 eV for the response functions, the spectral method, and 72 frequency points are adopted; (4) The Bethe–Salpeter equation is solved, where 22 highest occupied valence bands and 22 lowest unoccupied conduction bands are included.

3. Results and Discussion

3.1. Structural and Electronic Properties

Single-layer $GaInSe_3$ displays a 2D hexagonal unit cell with an in-plane constant of a = 3.95 Å (Figure 1a). Single-layer $GaInSe_3$ is stacked by Se-In-Se-Ga-Se atomic layers along the z-direction (Figure 1a), with an effective thickness of ~1 nm (Figure S1). Due to the asymmetric structure, single-layer $GaInSe_3$ exhibits an inside electric dipole (field) along the z-direction. The calculated electric dipoles are 9.36, 9.29, 9.26, 9.07, and 9.00 (10^{-2} e·Å) for −2%, −1%, 0%, +1%, and +2% biaxial strains, respectively. Hence, the inside dipole will play an important role in separating the generated holes and electrons. The large inside electric dipole produces a significant vacuum level difference ΔΦ between the bottom Ga-Se layer and the top Se-In-Se layer (Figure 1b and Figure S2 and Table S1).

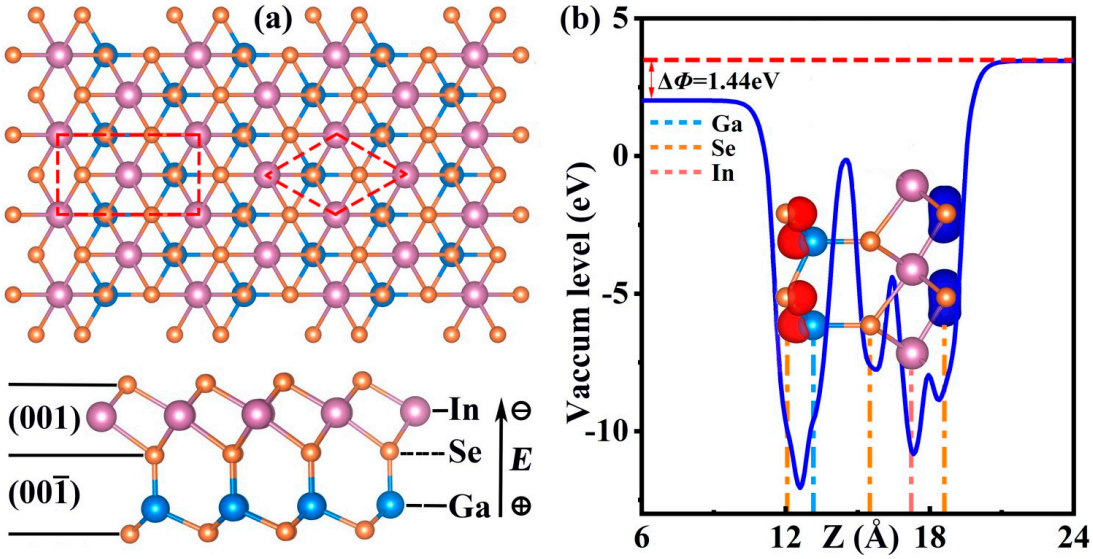

Figure 1. (**a**) The top and side views, where the rhombus denotes the primitive cell and the rectangle represents the orthogonal supercell. (**b**) The vacuum level difference of unstrained single-layer $GaInSe_3$, where the inset is the charge distribution of CBM (red) and VBM (blue). The red dashed horizontal lines are auxiliary lines. The solid blue curve shows the change in vacuum level.

The stability of unstrained single-layer $GaInSe_3$ has been investigated [15], and here we study its stability under biaxial strains. From −2% to 2% biaxial strains, only very small imaginary frequencies appear near the Γ point, and they could be eliminated gradually by enlarging the supercell [36], expressing good dynamic stability (Figure S3). Single-layer $GaInSe_3$ under biaxial strains from −2 to +2% exhibits free energy fluctuating around −160 eV and maintains the integrity of structural frames throughout the simulation process (Figures S4 and S5), proving thermal stability at 300 K. The theoretical elastic constants C_{ij} (Table S2) satisfy the Born–Huang mechanical stability criterion of lattice dynamics [37–39]: $C_{11} > 0$ and $C_{11} - C_{12} > 0$ suggesting mechanical stability. What is more, the total energy under the considered strain is very close to that at the ground state (Figure S6). Therefore, the dynamic stability, mechanical stability, and thermal stability under the considered biaxial strains have shown that single-layer $GaInSe_3$ can be realized in experiments.

A quasi-direct energy gap appears for single-layer $GaInSe_3$ under biaxial strains from −2% to +2%. Bandgaps are 1.28 eV for −2%, 1.25 eV for −1%, 1.21 eV for 0%, 1.16 eV for +1%, and 1.11 eV for +2% strain (Figure 2a–d and Figure S7). Notably, the moderate

bandgaps of single-layer $GaInSe_3$ are very helpful for visible light absorption. Furthermore, due to the vacuum level difference between the top and bottom surfaces, the VBM of unstrained single-layer $GaInSe_3$ is located at the top Se-In-Se trilayer—more precisely, at the highest Se atomic layer. Its CBM is mainly seated in the bottom Ga-Se bilayer (Figure 1b). Thus, the CBM and VBM are spatially separated, thus decreasing the electron–hole binding rate and improving the photocatalytic performance. The separated CBM and VBM also appear in single-layer $GaInSe_3$ under biaxial strains from −2% to 2% (Figure S8).

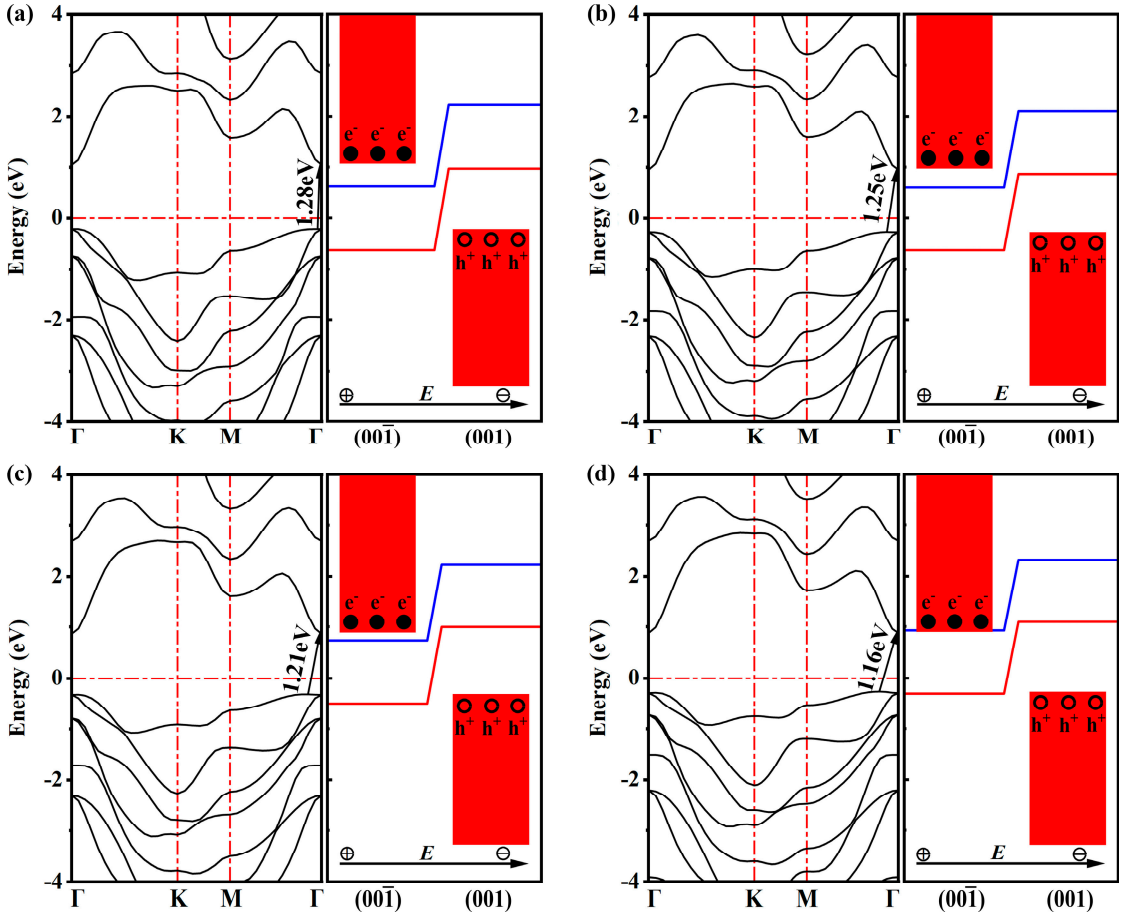

Figure 2. The electronic band structure (**Left**) and water-splitting property (**Right**) of single-layer $GaInSe_3$ under biaxial strains of (**a**) −2%, (**b**) −1%, (**c**) 0%, and (**d**) +1% obtained via HSE06. The upper and lower red columns denote the CBM and the VBM, respectively. The blue and red lines represent the redox potentials of H^+/H_2 and H_2O/O_2, respectively.

In addition, the spin–orbital coupling (SOC) has little influence on the electronic property of single-layer $GaInSe_3$ (Figure S9). The bandgaps at the G_0W_0 level are presented in Figure S10. Since the bandgaps of 2D materials are underestimated by PBE and overestimated by G_0W_0 [16], only the HSE06 bandgaps are focused on herein.

3.2. Band Alignment for Water-Splitting

As for water-splitting by sunlight, the most important prerequisite is that the aligned CBM level is higher than the H^+/H_2 reduction potential (E_{H^+/H_2}), while the aligned VBM level is below the O_2/H_2O oxidation potential (E_{O_2/H_2O}). Herein, the band edges are aligned using the method proposed by Toroker et al. [40] and revised by Yang et al. [10]. Considering the charge location of CBM and VBM (Figure 1b), the hydrogen evolution reactions (HERs) of single-layer $GaInSe_3$ take place on the Ga atomic layer, and the oxygen evolution reactions (OERs) mainly occur on the highest Se atomic layer. From

−2% to +2% biaxial strains, the band edges of single-layer $GaInSe_3$ are favorable for OERs (Figures 2a–d and S7). However, the band edges under +1% and +2% tensile biaxial strains are unfavorable for HERs. As a result, single-layer $GaInSe_3$ under biaxial strains from −2% to 0% can accomplish both HERs and OERs.

The overpotentials, including $\chi(H_2)$ and $\chi(O_2)$, which, respectively, scale the water-splitting abilities of HERs and OERs, are further studied (Table 1). The $\chi(H_2)$ ($\chi(O_2)$) is the potential difference between the aligned CBM (VBM) level and the H^+/H_2 (O_2/H_2O) potential. Under biaxial strains of −2% and −1%, the $\chi(H_2)$ values are larger than 0.2 eV, and the $\chi(O_2)$ values are larger than 0.6 eV, indicating good HER and OER ability [10]. In addition, the potential energies of photogenerated carriers (U_e and U_h) are also calculated to reveal the HER and OER abilities [41,42], also suggesting good HER and OER ability for single-layer $GaInSe_3$ at −2% and −1% biaxial strain.

Table 1. The overpotentials of HER ($\chi(H_2)$, U_e) and OER ($\chi(O_2)$, U_h) (eV) via HSE06 at pH = 0.

	$\chi(H_2)$	$\chi(O_2)$	U_e	U_h
−2%	0.46	1.03	0.46	2.26
−1%	0.30	1.17	0.30	2.40
0%	0.12	1.27	0.12	2.50

3.3. Optical Absorption and Exciton Binding Energy

For water-splitting, the photocatalysts should absorb as much as solar energy. Herein, the G_0W_0-BSE method is applied to study the absorption coefficient [32–35,43]. Due to the existence of a vacuum, the effective thickness is considered [44]. Calculations reveal that the first absorption peaks of $GaInSe_3$ under biaxial strains of −2%, −1%, and 0% are located at 1.57, 1.50, and 1.39 eV, respectively (Figure 3a). From −2% to 0% biaxial strains, single-layer $GaInSe_3$ exhibits multiple visible optical absorption peaks, and the maximum optical absorption reaches up to ~ 3×10^5 cm^{-1}, apparently stronger than that of other typical 2D photocatalysts such In_2Se_3 [45]. It is not difficult to find that the maximum optical absorption is increasing with the decreasing compressive biaxial strain. Moreover, the optical absorption spectra are red-shifted with the decreasing compressive biaxial strain. On the other hand, the square transition dipole matrix elements (P^2) between the top VB and the bottom CB are calculated via HSE06 [46]. From −2% to 0% biaxial strains, the maximum P^2 appears near the Γ point and approaches 20 $Debye^2$ (Figure 3b). The allowed optical transition further promises infrared and visible light absorption.

Water-splitting reactions require separated photogenerated electrons and holes. The exciton binding energy is an important parameter by which to measure the separation efficiency of charge carriers. Considering the quasi-direct bandgap of single-layer $GaInSe_3$, the exciton binding energy E_b is the energy difference between the first optical bandgaps (Figure 3a) and quasi-direct bandgaps (Figure S10). The quasi-direct bandgaps of single-layer $GaInSe_3$ under biaxial strains from −2%, −1%, and 0% are 2.03, 2.07, and 2.13 eV, respectively. The corresponding E_b values are 0.46, 0.57, and 0.74 eV, and lower than those of 2D photocatalysts, e.g., In_2Se_3 (0.69 eV) [10] and WSSe (0.82 eV) [17]. First, the relatively smaller exciton binding energies could be attributed to the separated CBM and VBM. Secondly, the inside electric field could play a big role in reducing the exciton binding energies.

3.4. Transport Mobility

The recombination rate of charge carriers is further investigated by including carrier mobility. Expressly, higher mobility means a lower recombination possibility. Herein, The carrier mobility is calculated using the deformation potential (DP) theory [47,48]:

$$\mu_{2D} = \frac{e\hbar^3 C_{2D}}{k_B T m^* m_d E_d^2}.$$

Here, e is the electron charge, $\hbar$ is the reduced Planck constant, C_{2D} is the elastic constant, k_B is the Boltzmann constant, and T is the room temperature (300 K). m^* is the effective mass and can be written as $\frac{1}{m^*} = \frac{1}{\hbar^2}\left|\frac{\partial^2 E(k)}{\partial k^2}\right|$. The average effective mass m_d is expressed as $m_d = \sqrt{m_x^* m_y^*}$. The symbol E_d represents the deformation potential constant. The fittings for effective masses m^* and deformation potential constants E_d are listed in Figures S11–S16. Herein, the E_d values are obtained with the consideration of VBM and CBM distribution (Figure 1b). Specifically, the E_d value of generated holes is taken as the slope of the linear fitting between $(E_{VBM} - \Phi_{top})$ and strain ε. E_d of generated electrons is taken as the slope of the linear fitting between $(E_{VBM} - \Phi_{bottom})$ and ε. The calculated effective masses m^*, elastic constants C_{2D}, and deformation potential constants E_d are summarized in Table 2.

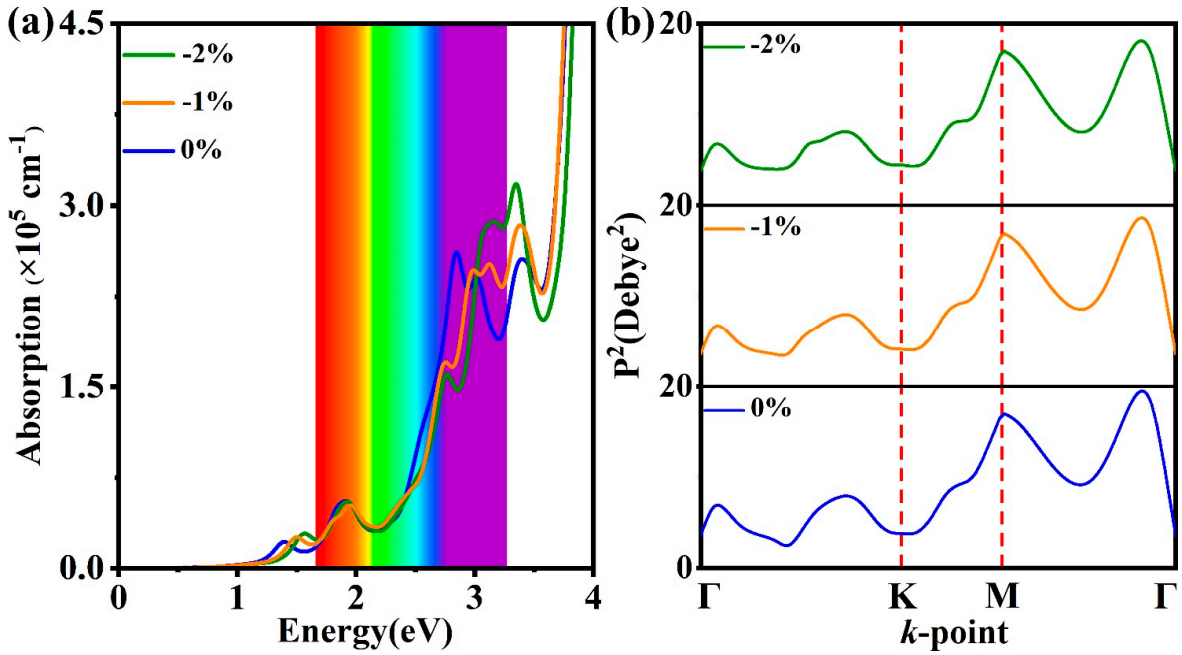

Figure 3. (**a**) Frequency-dependent absorption coefficients of single-layer $GaInSe_3$ under biaxial strains of −2%, −1%, and 0% by G_0W_0-BSE. (**b**) Transition dipole moment of single-layer $GaInSe_3$ under biaxial strains of −2%, −1%, and 0% by HSE06.

Table 2. Elastic modulus C_{2D} ($N{\cdot}m^{-1}$), effective mass m^* (m_e), deformation potential E_d (eV), and carrier mobility μ ($cm^2{\cdot}V^{-1}{\cdot}s^{-1}$) along the x and y directions of single-layer $GaInSe_3$ under biaxial strains from −2% to 0%.

Stain	Direction	Species	m^*	C_{2D}	E_d	μ
−2%	x	Electron	0.16	85.61	4.66	3455.11
		Hole	0.40	85.61	5.08	95.86
	y	Electron	0.16	85.61	6.22	2901.05
		Hole	3.71	85.61	6.74	8.85
−1%	x	Electron	0.15	82.13	7.79	1205.60
		Hole	0.35	82.13	3.75	342.64
	y	Electron	0.15	82.13	7.70	1232.79
		Hole	2.96	82.13	5.38	19.95
0%	x	Electron	0.15	78.36	7.40	1281.00
		Hole	0.34	78.36	2.64	748.44
	y	Electron	0.15	78.36	7.58	1223.19
		Hole	2.58	78.36	5.71	21.11

For unstrained single-layer $GaInSe_3$, the electron effective masses (0.15 m_e) and elastic constants (78.36 N/m) along the x and y directions are both isotropic. Due to the small electron-effective masses, a relatively large mobility (~1250 $cm^2 \cdot V^{-1} \cdot s^{-1}$) of photogenerated electrons is obtained. For comparison, recently discovered 2D photocatalysts display electron mobility: 1049 $cm^2 \cdot V^{-1} \cdot s^{-1}$ for GeS [49] and 601 $cm^2 \cdot V^{-1} \cdot s^{-1}$ for $CoGeSe_3$ [50]. Moreover, apparent hole mobility anisotropy between the x and y directions appears owing to various effective masses and deformation potential constants. Another prominent characteristic is that the generated electrons run much faster than the generated holes, which promises an effective separation of photogenerated electrons and holes. Under −2% and −1% biaxial strains, effective separation of photogenerated carriers inside single-layer $GaInSe_3$ still exists, and then ensures the occurrence of photocatalytic reactions.

3.5. OER and HER

Although single-layer $GaInSe_3$ exhibits a suitable band edge for redox reaction under biaxial strains from −2% to 0%, it is necessary to calculate the Gibb free energy in OER and HER. Combined with the analysis of the charge density of VBM and CBM, the HER will take place on the bottom Ga-Se bilayer, and the OER will take place on the highest Se atomic layer. The OER is divided into four steps, as follows in Equations (1)–(4) [2,51]:

$$* + H_2O \rightarrow OH^* + H^+ + e^- \quad (1)$$

$$OH^* \rightarrow O^* + H^+ + e^- \quad (2)$$

$$O^* + H_2O \rightarrow OOH^* + H^+ + e^- \quad (3)$$

$$OOH^* \rightarrow * + O_2 + H^+ + e^-. \quad (4)$$

The two steps of HER are given by Equations (5) and (6) [2,51]:

$$* + H^+ + e^- \rightarrow H^* \quad (5)$$

$$H^* + H^+ + e^- \rightarrow * + H_2, \quad (6)$$

where * indicates the adsorbed material (single-layer $GaInSe_3$), and OH^*, O^*, OOH^*, and H^* represent the adsorbed intermediates. For all the calculations, spin polarization is taken into account. By considering the zero-point energy and entropy corrections, the expression of ΔG can be written as $\Delta G = \Delta E_{ads} + \Delta E_{ZPE} - T\Delta S$, where ΔE_{ads} is the adsorption energy, and ΔE_{ZPE} and ΔS are the difference of zero-point energy and entropy difference between the adsorbed state and the gas phase, respectively. T represents the room temperature of 300 K.

For each reaction of oxidation generation, ΔG can be written as follows in Equations (7)–(10) [2,51]:

$$\Delta G_1 = G_{OH^*} + \frac{1}{2}G_{H_2} - G^* - G_{H_2O} + \Delta G_U - \Delta G_{pH} \quad (7)$$

$$\Delta G_2 = G_{O^*} + \frac{1}{2}G_{H_2} - G_{OH^*} + \Delta G_U - \Delta G_{pH} \quad (8)$$

$$\Delta G_3 = G_{OOH^*} + \frac{1}{2}G_{H_2} - G_{O^*} - G_{H_2O} + \Delta G_U - \Delta G_{pH} \quad (9)$$

$$\Delta G_4 = G^* + \frac{1}{2}G_{H_2} + G_{O_2} - G_{OOH^*} + \Delta G_U - \Delta G_{pH}, \quad (10)$$

where ΔG_U $(\Delta G_U = -eU)$ denotes extra potential bias provided by an electron in the electrode, and U is the electrode potential relative to the standard hydrogen electrode (SHE). $\Delta G_{pH}(\Delta G_{pH} = k_B T \times ln10 \times \mathrm{pH})$ represents the free energy contributed in different pH.

Because of the required large computational resources, only the OER and HER of unstrained single-layer $GaInSe_3$ are studied. The optimized configurations of the OH^*, O^*, and OOH^* intermediates are given (Figure S17). The formation of OH^*, O^*, and OOH^* are all endothermic in the absence of solar light (Figure 4a). The third step is a rate-limiting step involving the OOH^* formation and has a Gibbs free energy change of 2.25 eV. Therefore, the minimum external potential for OER converted into exothermic heat is 2.25 V. As shown in Table 1, for unstrained single-layer $GaInSe_3$, the external electric potential supplied by the photogenerated hole is 2.50 V $(U_h' = U_h/e)$, indicating that OER can proceed smoothly without a co-catalyst.

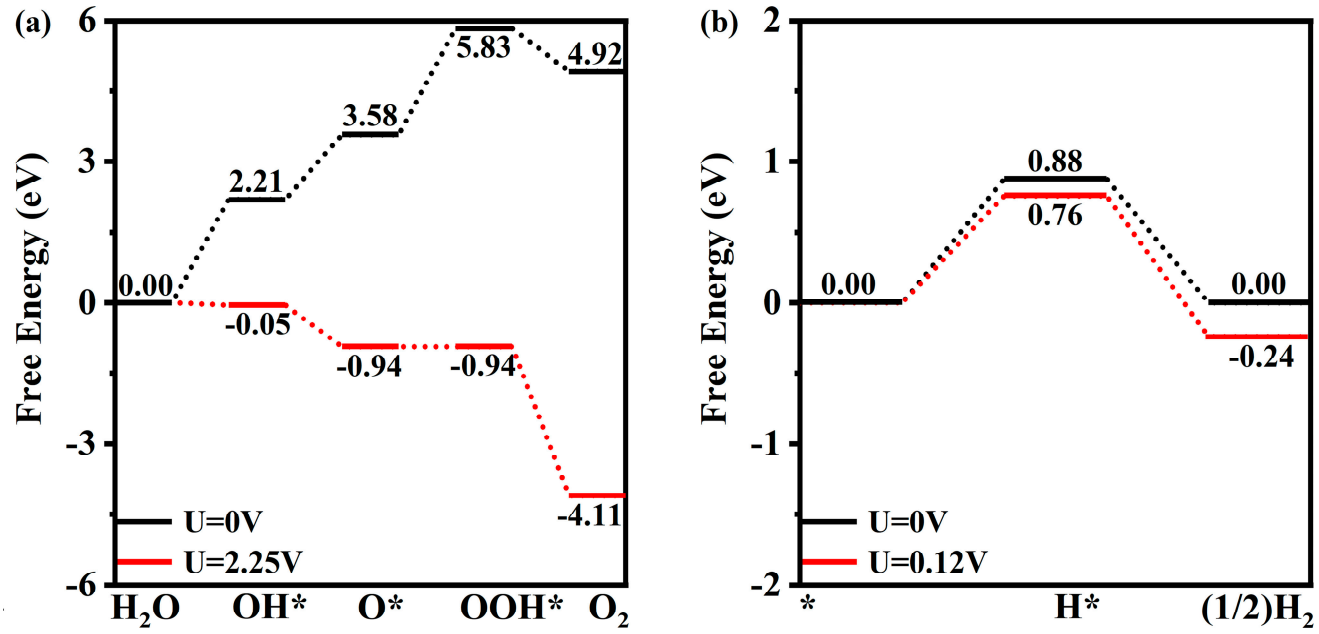

Figure 4. (**a**) The Gibbs free energy change of OER on the Se atomic plane; (**b**) that of HER on the bottom Ga atomic layer of unstrained single-layer $GaInSe_3$ at pH = 0. The * indicates the adsorbed material.

On the other hand, the Gibbs free energy profile of HER is displayed in Figure 4b. The optimized configurations of the H^* intermediate are given (Figure S18), where the HER active site is the Ga atomic layer. In the absence of light irradiation, the first and second steps are endothermic and exothermic with ΔG = 0.88 eV, respectively. Therefore, the minimum external potential for a successful HER is 0.88 V. However, the external electric potential of unstrained single-layer $GaInSe_3$ (Table 1) supplied by the photogenerated electrons is 0.12 V. In this condition, the first step involving the H* formation is also endothermic, with ΔG = 0.76 eV, indicating that HER cannot proceed successfully without a cocatalyst. Fortunately, in previous experiments, the HER energy barrier could be lowered to less than 0.1 eV [52].

3.6. Solar-to-Hydrogen Efficiency

Here, we investigate the solar conversion efficiency of single-layer $GaInSe_3$ in water-spitting reactions. Generally, the η_{STH} value is obtained by timing the light absorption efficiency (η_{abs}) and the carrier utilization efficiency (η_{cu}). The η_{abs} value is calculated via Equation (11):

$$\eta_{abs} = \frac{\int_{E_g}^{\infty} P(\hbar w) d(\hbar w)}{\int_{0}^{\infty} P(\hbar w) d(\hbar hw)}, \quad (11)$$

where $P(\hbar w)$ is the AM1.5G solar energy flux at the photon energy $\hbar w$, and E_g is the bandgap by HSE06 (Figures 2 and S6). Due to the narrower bandgap, the η_{abs} values of single-layer $GaInSe_3$ under biaxial strains from −2% to 0% exceed 70%.

The η_{cu} is calculated via Equation (12):

$$\eta_{cu} = \frac{\Delta G \int_E^\infty \frac{P(\hbar w)}{\hbar w} d(\hbar w)}{\int_{E_g}^\infty P(\hbar w) d(\hbar w)}, \quad (12)$$

where $\Delta G = 1.23$ eV is the potential difference for photocatalytic water-splitting. The symbol E is the actual energy barrier for photocatalytic water-splitting and is determined via Equation (13):

$$E = \begin{cases} E_g, \ (\chi(H_2) \geq 0.2, \chi(O_2) \geq 0.60) \\ E_g + 0.2 - \chi(H_2), \ (\chi(H_2) < 0.2, \chi(O_2) \geq 0.60) \\ E_g + 0.6 - \chi(O_2), \ (\chi(H_2) \geq 0.2, \chi(O_2) < 0.60) \\ E_g + 0.8 - \chi(H_2) - \chi(O_2), \ (\chi(H_2) < 0.2, \chi(O_2) < 0.60) \end{cases}. \quad (13)$$

The overpotentials of $\chi(H_2)$ and $\chi(O_2)$ values are listed in Table 1. Furthermore, the η_{cu} values from −2% to 0% are found to surpass 70%. Herein, the STH efficiencies (η_{STH}) under biaxial strains of −2%, −1%, and 0% via Equation (14) are 44.18%, 45.85%, and 44.00%, respectively.

$$\eta_{STH} = \eta_{abs} \times \eta_{cu} \quad (14)$$

The η_{STH} is further corrected by the inside electric field via Equation (15):

$$\eta'_{STH} = \eta_{STH} \times \frac{\int_0^\infty P(\hbar w) d(\hbar w)}{\int_0^\infty P(\hbar w) d(\hbar w) + \Delta\Phi \int_{E_g}^\infty \frac{P(\hbar w)}{\hbar w} d(\hbar w)}, \quad (15)$$

where $\Delta\Phi$ is the potential difference between the vacuum level at the top and bottom surfaces (Table 1). Very excitingly, the corrected STH efficiency (η'_{STH}) of single-layer $GaInSe_3$ under biaxial strains of −2%, −1%, and 0% reaches 31.20%, 32.50%, and 31.29%, respectively, far surpassing the commercial standard (10%) [10] and showing glorious prospects for commercial application (Table 3). It should be pointed out that we assume the external quantum efficiency of 100% for the overall water-splitting reaction; that is, the obtained STH efficiency is a theoretical limitation. Lower SHT efficiency was obtained in the experiments. Specifically, the low U_e of single-layer $GaInSe_3$ under zero strain suggests possible photo corrosion, which will reduce the STH efficiency.

Table 3. The energy conversion efficiency of light absorption (η_{abs}), carrier utilization (η_{cu}), solar-to-hydrogen (STH) (η_{STH}), and corrected STH (η'_{STH}) of single-layer $GaInSe_3$ under biaxial strains of −2%, −1%, and 0%.

Species	Strain	η_{abs}(%)	η_{cu}(%)	η_{STH}(%)	η'_{STH}(%)
pH = 0	−2%	71.02	79.63	44.18	31.20
	−1%	72.74	78.80	45.85	32.50
	0%	75.05	70.93	44.00	31.29

4. Conclusions

The solar water-splitting properties of single-layer $GaInSe_3$ have been studied. Under biaxial strains from −2% to +2%, single-layer $GaInSe_3$ exhibits stable structures and moderate bandgaps from 1.11 to 1.28 eV. Under biaxial strains from −2% to 0%, single-layer $GaInSe_3$ holds suitable band edges for photocatalytic water-splitting at pH = 0, and the strong visible optical absorption is up to ~3×10^5 cm^{-1}. Meanwhile, the charge carriers can be effectively separated due to the strong inside electric field and high electron mobility. More attractively, the solar energy conversion efficiency surpasses 30%. The OER of

unstrained single-layer $GaInSe_3$ can proceed without a co-catalyst. Therefore, single-layer $GaInSe_3$ is a promising photo-catalyst material for water-splitting.

Supplementary Materials: The following supporting information can be downloaded at https://www.mdpi.com/article/10.3390/molecules28196858/s1. Figure S1: Effective thickness; Figure S2 and Table S1: Vacuum level difference; Figure S3: Phonon dispersion; Figures S4 and S5:Thermal stability; Figure S6: Total energy under the considered strain; Figure S7: HSE06 band structure and the band alignment under the −2% biaxial strain; Figure S8: Spatial distribution of CB and VB; Figure S9: PBE band with and without SOC; Figure S10: G_0W_0 band; Figures S11–S16: Quadratic and linear fittings for transport mobility; Figure S17: Configurations of OH*, O* and OOH*; Figure S18: Configurations of H*; Table S2: Elastic constants; Table S3: Free energy related physical quantities.

Author Contributions: Conceptualization, L.-L.L.; Methodology, Y.-F.W. and X.-Z.W.; Software, X.-Z.W.; Validation, X.-Z.W.; Formal analysis, L.-L.L.; Resources, X.-Z.W.; Data curation, R.-F.T., D.-F.L., M.-X.T., B.-Z.M. and Z.-Q.H.; Writing—original draft preparation, L.-L.L.; Writing—review and editing, L.-L.L. and S.-F.W.; Supervision, Y.-F.W. All authors have read and agreed to the published version of the manuscript.

Funding: This research was funded by the Science and Technology Research Program of Chongqing Municipal Education Commission (Grant No. KJZD-K202301207) and the National Natural Science Foundation of China (Grant Nos. 12064019 and U2030116).

Institutional Review Board Statement: Not applicable.

Informed Consent Statement: Not applicable.

Data Availability Statement: Not applicable.

Conflicts of Interest: The authors declare no conflict of interest.

Sample Availability: Samples of the compounds are available from the authors.

References

1. Fujishima, A.; Honda, K. Electrochemical photolysis of water at a semiconductor electrode. *Nature* **1972**, *238*, 37–38. [CrossRef] [PubMed]
2. Zhang, W.-X.; Hou, J.-T.; Bai, M.; He, C.; Wen, J.-R. Construction of novel ZnO/Ga_2SSe (GaSe) vdW heterostructures as efficient catalysts for water splitting. *Appl. Surf. Sci.* **2023**, *634*, 157648. [CrossRef]
3. Li, Y.-F.; Feng, Y.-C.; Bai, H.; Liu, J.-S.; Hu, D.-Y.; Fan, J.-Y.; Shen, H.-L. Enhanced visible-light photocatalytic performance of black TiO_2/SnO_2 nanoparticles. *J. Alloys Compd.* **2023**, *960*, 170672. [CrossRef]
4. Schneider, J.; Matsuoka, M.; Takeuchi, M.; Zhang, J.-L.; Horiuchi, Y.; Anpo, M.; Bahnemann, D.-W. Understanding TiO_2 photocatalysis: Mechanisms and materials. *Chem. Rev.* **2014**, *114*, 9919–9986. [CrossRef]
5. Cardona, M. Optical Properties and Band Structure of $SrTiO_3$ and $BaTiO_3$. *Phys. Rev.* **1965**, *140*, A651. [CrossRef]
6. Singh, A.K.; Mathew, K.; Zhuang, H.L.; Hennig, R.G. Computational Screening of 2D Materials for Photocatalysis. *J. Phys. Chem. Lett.* **2015**, *6*, 1087–1098. [CrossRef] [PubMed]
7. Jin, H.; Wang, T.; Gong, Z.R.; Long, C.; Dai, Y. Prediction of an extremely long exciton lifetime in Janus-MoSTe monolayer. *Nanoscale* **2018**, *10*, 19310–19315. [CrossRef] [PubMed]
8. Liu, Y.; Jiang, Z.; Jia, J.; Robertson, J.; Guo, Y. 2D $WSe_2/MoSi_2N_4$ type-II heterojunction with improved carrier separation and recombination for photocatalytic water splitting. *Appl. Surf. Sci.* **2023**, *611*, 155674. [CrossRef]
9. Wang, P.; Liu, H.; Zong, Y.; Wen, H.; Xia, J.B.; Wu, H.B. Two-Dimensional In_2X_2X' (X and X′ = S, Se, and Te) Monolayers with an Intrinsic Electric Field for High-Performance Photocatalytic and Piezoelectric Applications. *ACS Appl. Mater. Interfaces* **2021**, *13*, 34178–34187. [CrossRef]
10. Fu, C.F.; Sun, J.; Luo, Q.; Li, X.; Hu, W.; Yang, J. Intrinsic Electric Fields in Two-dimensional Materials Boost the Solar-to-Hydrogen Efficiency for Photocatalytic Water Splitting. *Nano Lett.* **2018**, *18*, 6312–6317. [CrossRef]
11. Li, L.; Salvador, P.A.; Rohrer, G.S. Photocatalysts with internal electric fields. *Nanoscale* **2014**, *6*, 24–42. [CrossRef] [PubMed]
12. Ding, W.; Zhu, J.; Wang, Z.; Gao, Y.; Xiao, D.; Gu, Y.; Zhang, Z.; Zhu, W. Prediction of intrinsic two-dimensional ferroelectrics in In_2Se_3 and other III_2-VI_3 van der Waals materials. *Nat. Commun.* **2017**, *8*, 14956. [CrossRef]
13. Zhou, Y.; Wu, D.; Zhu, Y.; Cho, Y.; He, Q.; Yang, X.; Herrera, K.; Chu, Z.; Han, Y.; Downer, M.C.; et al. Out-of-Plane Piezoelectricity and Ferroelectricity in Layered α-In2Se3 Nanoflakes. *Nano Lett.* **2017**, *17*, 5508–5513. [CrossRef] [PubMed]
14. Ma, X.-C.; Wu, X.; Wang, H.-D.; Wang, Y.-C. A Janus MoSSe monolayer: A potential wide solar-spectrum water-splitting photocatalyst with a low carrier recombination rate. *J. Mater. Chem. A* **2018**, *6*, 2295–2301. [CrossRef]

15. Vu, T.V.; Hieu, N.N.; Lavrentyev, A.A.; Khyzhun, O.Y.; Lanh, C.V.; Kartamyshev, A.I.; Phuc, H.V.; Hieu, N.V. Novel Janus $GaInX_3$ (X = S, Se, Te) single-layers: First-principles prediction on structural, electronic, and transport properties. *RSC Adv.* **2022**, *12*, 7973–7979. [CrossRef]
16. Zhuang, H.L.; Hennig, R.G. Single-Layer Group-III Monochalcogenide Photocatalysts for Water Splitting. *Chem. Mater.* **2013**, *25*, 3232–3238. [CrossRef]
17. Ju, L.; Bie, M.; Tang, X.; Shang, J.; Kou, L.-Z. Janus WSSe Monolayer: An Excellent Photocatalyst for Overall Water Splitting. *ACS Appl. Mater. Interfaces* **2020**, *12*, 29335–29343. [CrossRef]
18. Kresse, G.; Hafner, J. Ab initio molecular dynamics for liquid metals. *Phys. Rev. B* **1993**, *47*, 558–561. [CrossRef]
19. Kresse, G.; Furthmüller, J.; Hafner, J. Ab initio molecular-dynamics simulation of the liquid-metal–amorphous-semiconductor transition in germanium. *Phys. Rev. B* **1994**, *49*, 14251–14269. [CrossRef]
20. Kresse, G.; Furthmüller, J. Efficient iterative schemes for ab initio total-energy calculations using a plane-wave basis set. *Phys. Rev. B* **1996**, *54*, 11169–11186. [CrossRef]
21. Kresse, G.; Joubert, D. From ultrasoft pseudopotentials to the projector augmented-wave method. *Phys. Rev. B* **1999**, *59*, 1758. [CrossRef]
22. Blöchl, P.E. Projector augmented-wave method. *Phys. Rev. B* **1994**, *50*, 17953. [CrossRef] [PubMed]
23. Perdew, J.P.; Burke, K.; Ernzerhof, M. Generalized gradient approximation made simple. *Phys. Rev. Lett.* **1996**, *77*, 3865. [CrossRef]
24. Marom, N.; Tkatchenko, A.; Rossi, M.; Gobre, V.V.; Hod, O.; Scheffler, M.; Kronik, L. Dispersion Interactions with Density-Functional Theory: Benchmarking Semiempirical and Interatomic Pairwise Corrected Density Functionals. *J. Chem. Theory Comput.* **2011**, *7*, 3944–3951. [CrossRef]
25. Perdew, J.P.; Ernzerhof, M.; Burke, K. Rationale for mixing exact exchange with density functional approximations. *J. Chem. Phys.* **1996**, *105*, 9982–9985. [CrossRef]
26. Heyd, J.; Scuseria, G.E.; Ernzerhof, M. Hybrid functionals based on a screened Coulomb potential. *J. Chem. Phys.* **2003**, *118*, 8207–8215. [CrossRef]
27. Heyd, J.; Peralta, J.E.; Scuseria, G.E.; Martin, R.L. Energy band gaps and lattice parameters evaluated with the Heyd-Scuseria-Ernzerhof screened hybrid functional. *J. Chem. Phys.* **2005**, *123*, 174101. [CrossRef]
28. Mostofi, A.A.; Yates, J.R.; Pizzi, G.; Lee, Y.-S.; Souza, I.; Vanderbilt, D.; Marzari, N. An updated version of wannier90: A tool for obtaining maximally-localised Wannier functions. *Comput. Phys. Commun.* **2014**, *185*, 2309–2310. [CrossRef]
29. Wu, X.; Vanderbilt, D.; Hamann, D.R. Systematic treatment of displacements, strains, and electric fields in density-functional perturbation theory. *Phys. Rev. B* **2005**, *72*, 035105. [CrossRef]
30. Togo, A.; Oba, F.; Tanaka, I. First-principles calculations of the ferroelastic transition between rutile-type and $CaCl_2$-type SiO_2 at high pressures. *Phys. Rev. B* **2008**, *78*, 134106. [CrossRef]
31. Togo, A.; Tanaka, I. First principles phonon calculations in materials science. *Scr. Mater.* **2015**, *108*, 1–5. [CrossRef]
32. Hybertsen, M.S.; Louie, S.G. Electron correlation in semiconductors and insulators: Band gaps and quasiparticle energies. *Phys. Rev. B* **1986**, *34*, 5390–5413. [CrossRef] [PubMed]
33. Albrecht, S.; Reining, L.; Del Sole, R.; Onida, G. Ab initio calculation of excitonic effects in the optical spectra of semiconductors. *Phys. Rev. Lett.* **1998**, *80*, 4510. [CrossRef]
34. Benedict, L.X.; Shirley, E.L.; Bohn, R.B. Optical absorption of insulators and the electron-hole interaction: An ab initio calculation. *Phys. Rev. Lett.* **1998**, *80*, 4514. [CrossRef]
35. Rohlfing, M.; Louie, S.G. Electron-Hole Excitations in Semiconductors and Insulators. *Phys. Rev. Lett.* **1998**, *81*, 2312. [CrossRef]
36. Zhang, Z.-W.; Chen, G.-X.; Song, A.-Q.; Cai, X.-L.; Yu, W.-Y.; Jia, X.-T.; Jia, Y. Optoelectronic properties of bilayer van der Waals $WSe_2/MoSi_2N_4$ heterostructure: A first-principles study. *Physica E.* **2022**, *144*, 115429. [CrossRef]
37. Born, M.; Huang, K.; Lax, M. Dynamical Theory of Crystal Lattices. *Am. J. Phys* **1955**, *23*, 474. [CrossRef]
38. Mouhat, F.; Coudert, F.X. Necessary and sufficient elastic stability conditions in various crystal systems. *Phys. Rev. B* **2014**, *90*, 224104. [CrossRef]
39. Shi, W.; Wang, Z. Mechanical and electronic properties of Janus monolayer transition metal dichalcogenides. *J. Phys. Condens. Matter.* **2018**, *30*, 215301. [CrossRef]
40. Toroker, M.C.; Kanan, D.K.; Alidoust, N.; Isseroff, L.Y.; Liao, P.; Carter, E.A. First principles scheme to evaluate band edge positions in potential transition metal oxide photocatalysts and photoelectrodes. *Phys. Chem. Chem. Phys.* **2011**, *13*, 16644–16654. [CrossRef]
41. Nan, G.T.; Zhang, W.; Yan, X.J.; Qin, X.; Wu, S.; Tang, R.F.; Tang, M.X.; Hu, L.; Liu, L.L.; Wang, S.F.; et al. $ZnGeSe_2$ monolayer: Water-splitting photocatalyst with ultrahigh solar conversion efficiency. *Phys. Chem. Chem. Phys.* **2023**, *25*, 24594–24602. [CrossRef] [PubMed]
42. Qiao, M.; Liu, J.-S.; Wang, Y.; Li, Y.F.; Chen, Z.F. $PdSeO_3$ Monolayer: Promising Inorganic 2D Photocatalyst for Direct Overall Water Splitting Without Using Sacrificial Reagents and Cocatalysts. *J. Am. Chem. Soc.* **2018**, *140*, 12256–12262. [CrossRef] [PubMed]
43. Ma, C.; Liu, T.; Chang, Q. Study on the electronic structures and optical absorption of F center in the SrO crystal with G_0W_0–BSE. *Comput. Theor. Chem.* **2016**, *1080*, 79–83. [CrossRef]
44. Hu, L.; Wei, D.-S. Janus group-III chalcogenide monolayers and derivative type-II heterojunctions as water-splitting photocatalysts with strong visible-light absorbance. *J. Phys. Chem. C.* **2018**, *122*, 27795–27802. [CrossRef]

45. Zhao, P.; Ma, Y.-D.; Lv, X.-S.; Li, M.-M.; Huang, B.-B.; Dai, Y. Two-dimensional III_2-VI_3 materials: Promising photocatalysts for overall water splitting under infrared light spectrum. *Nano Energy* **2018**, *51*, 533–538. [CrossRef]
46. Meng, W.; Wang, X.; Xiao, Z.; Wang, J.; Mitzi, D.B.; Yan, Y. Parity-forbidden transitions and their impact on the optical absorption properties of lead-free metal halide perovskites and double perovskites. *J. Phys. Chem. Lett.* **2017**, *8*, 2999–3007. [CrossRef] [PubMed]
47. Qiao, J.; Kong, X.; Hu, Z.X.; Yang, F.; Ji, W. High-mobility transport anisotropy and linear dichroism in few-layer black phosphorus. *Nat. Commun.* **2014**, *5*, 4475. [CrossRef]
48. Bardeen, J.; Shockley, W. Deformation potentials and mobilities in non-polar crystals. *Phys. Rev.* **1950**, *80*, 72. [CrossRef]
49. Qiao, M.; Chen, Y.-L.; Wang, Y.; Li, Y.-F. The germanium telluride monolayer: A two dimensional semiconductor with high carrier mobility for photocatalytic water splitting. *J. Mater. Chem. A* **2018**, *6*, 4119–4125. [CrossRef]
50. Jalil, A.; Ilyas, S.-Z.; Agathopoulos, S.; Qureshi, A.; Ahmed, I.; Zhao, T.-K. 2D $CoGeSe_3$ monolayer as a visible-light photocatalyst with high carrier mobility: Theoretical prediction. *Appl. Surf. Sci.* **2021**, *565*, 150588. [CrossRef]
51. Nørskov, J.K.; Bligaard, T.; Logadottir, A.; Kitchin, J.R.; Chen, J.G.; Pandelov, S.; Stimming, U. Trends in the Exchange Current for Hydrogen Evolution. *J. Electrochem. Soc.* **2005**, *152*, J23. [CrossRef]
52. Zheng, Y.; Jiao, Y.; Jaroniec, M.; Qiao, S.Z. Advancing the Electrochemistry of the Hydrogen-Evolution Reaction through Combining Experiment and Theory. *Angew. Chem. Int.* **2014**, *54*, 52–65. [CrossRef] [PubMed]